Robocasting of controlled porous $CaSiO_3$–SiO_2 structures: Architecture – Strength relationship and material catalytic behavior

Mariano Casas-Luna[a], Jorge Alberto Torres-Rodríguez[a], Omar Uriel Valdés-Martínez[b], Nina Obradović[c], Karel Slámečka[a], Karel Maca[a], Jozef Kaiser[a], Edgar B. Montúfar[a], Ladislav Čelko[a]

[a] CEITEC – Central European Institute of Technology - Brno University of Technology, Purkyňova 123, 612 00, Brno, Czech Republic
[b] Universidad Autónoma Metropolitana, Iztapalapa, Av. San Rafael Atlixco 186, 09340, Mexico City, Mexico
[c] Institute of Technical Sciences of the Serbian Academy of Science and Arts, Knez Mihailova 35/IV, 11000, Belgrade, Serbia

Abstract: Wollastonite ($CaSiO_3$) based porous structures are useful in a wide range of applications including catalysis. Furthermore, the use of additive manufacturing techniques for the production of on-demand structures with controlled porosity are widely used for numerous materials. In the present work, $CaSiO_3$ was synthesized by co-precipitation method resulting in a fine $CaSiO_3$–SiO_2 powder, which was processed to fabricate regular porous structures using the robocasting technique. Cylindrical structures of 10 mm in diameter and 10 mm in height were robocast following two different arrangement patterns, i.e., orthogonal and honeycomb with two different pore sizes (350 and 500 μm). In general, the orthogonal structures showed better geometrical and dimensional accuracy than honeycomb ones. The compression test showed that orthogonal structures were more reliable, while the honeycomb structures exhibited higher compressive strength. The reasons are on the differences in porosity and pore architecture between them. Additionally, the catalytic properties of the $CaSiO_3$–SiO_2 powder were studied by the decomposition of isopropyl alcohol. The $CaSiO_3$–SiO_2 showed strong selective basic catalytic properties, leading on the dehydrogenation of the alcohol producing acetone with a yield up to 92% at 350 °C. In summary, the $CaSiO_3$–SiO_2 robocast structures have a significant potential for self-supporting catalytic reactors.

Keywords: Wollastonite, Silica, Robocasting, Catalytic activity, Compressive strength,

1. Introduction

Wollastonite is one of the calcium silicates with wide scientific and industrial applications. With a chemical formula of $CaSiO_3$, wollastonite possesses interesting properties, e.g., creep resistance, chemical inertness, thermal stability, low thermal expansion, and low thermal conductivity [1]. Wollastonite and its high-temperature polymorph pseudowollastonite (β-wollastonite, $Ca_3Si_3O_9$) are natural-resource minerals and for many years this calcium silicate was a mine residue useful as a thermal insulator [2] and as an additive mixture in the cement industry [3]. In the last decade, $CaSiO_3$ has been investigated for its ability to adsorb heavy metallic ions, e.g., Pb^{+2}, Cr^{+6} or Ni^{+2} [4, 5, 6]. Most recently, wollastonite has become suitable for reinforcing composites [7,8] and as a bone substitute in orthopedic applications owing to its bioactive properties [9,10]. Different methods are currently known for the production of synthetic wollastonite from various sources of calcium and silicon, e.g., synthesis *via* solid-state reaction [11,12], sol-gel method [13,14], hydrothermal synthesis [15], chemical precipitation [16,17], among others. Most of the wollastonite applications involve the use of bulk bodies or free-particles that exhibit as large specific surface area as possible without detriment of the mechanical stability. Thus, either for orthopedic implants, adsorbent filters,

water purification, catalysts, reinforcement fillers for composites, or in some cases as insulators, wollastonite porous structures can fulfill the design requirements in an environmentally sustainable manner [18,19].

Nowadays, one of the methods for the fabrication of controlled porous structures is additive manufacturing, which allows the processing of endless-list of materials to produce diverse shaped-structures with different degrees of open porosity. Among the additive manufacturing techniques, robocasting (direct ink writing) allows to design and rapidly fabricate any kind of powder materials in a form of injectable pastes into complex 3D shapes without the need of expensive tooling, dies, or lithographic masks [20].

Previously, robocasting has been successfully used to fabricate calcium phosphate porous structures reinforced with wollastonite [10]. Wollastonite improves the mechanical strength of calcium phosphates without compromising their biocompatibility, making possible to use the obtained biphasic structures as scaffolds for bone tissue engineering. Despite the potential use of wollastonite porous structures for catalysis, there are not studies devoted to the robocasting of wollastonite porous structures for such purpose. Therefore, this work is focused on the synthesis and processing of calcium silicate powder with a Ca/Si in equal ratio to obtain the wollastonite phase composition in order to manufacture porous structures with catalytic activity. Synthesis of the calcium silicate led to a composite ceramic based on $CaSiO_3$–SiO_2 system that was processed to create sets of predesign porous structures by means of robocasting technique. The resulted structures were compared in terms of their compressive-strength dependency on the pore geometry and size. Additionally, the catalytic activity of the obtained calcium silicate powder was evaluated in terms of the decomposition of isopropyl alcohol vapor. This reaction is commonly used as a model in studies of variations in catalytic activity and selectivity at the temperature range from 250 to 350 °C for nonmetallic catalysts. Additionally, the acid active sites were evaluated by NH_3 adsorption.

2. Materials and methods

2.1. Synthesis of $CaSiO_3$ powder

Calcium silicate powder was prepared by means of co-precipitation method using calcium nitrate, $Ca(NO_3)_2 \cdot 4H_2O$ (≥99%; Sigma Aldrich, Germany) and tetraethylorthosilicate (TEOS), $Si(OC_2H_5)_4$ (≥99%; Sigma Aldrich, Germany) as reactants. The reactants were separately dissolved in 500 mL of analytical-grade ethanol (Merck, Germany) to create two separate solutions containing the equal molar concentration of Ca and Si ions in order to keep a stoichiometric Ca/Si ratio for the formation of the $CaSiO_3$. Both solutions were mixed and kept under stirring for 30 min, then ammonium hydroxide solution (NH_4OH, 26% w/w solution in water, Sigma Aldrich, Germany) was added dropwise until the solution turned turbid and particles started to precipitate. The suspension was let to mature under stirring for 2 h. The obtained product was filtered and rinsed three times with distilled water to eliminate residues from the reactants. Finally, the obtained material was dried at 120 °C and calcined at 800 °C for 5 h to obtain a block that was milled in a vibration disk mill (RETSCH, Germany) at 1000 rpm for 100 s; the final powder was sieved at a particle size below 36 μm to obtain a conditioned powder for the robocasting.

2.2. Robocasting and sintering of porous $CaSiO_3$–SiO_2 structures

Robocasting technique was used to produce cylindrical samples of 10 mm in diameter and 10 mm in height. The sieved powder was mixed with a water-based solution of 40 wt % of pluronic F-127 (Sigma Aldrich, Germany) in a 1:1 wt ratio with the purpose of producing a

paste that was extruded using a robotic deposition apparatus (Pastecaster, Fundació CIM, Spain) at an extrusion rate of 8 $mm \cdot s^{-1}$, using a nozzle with an aperture of 410 μm. The samples were printed following different filling patterns named as honeycomb (hexagonal-like pores) and orthogonal (squared pores) patterns. The filling ratio of the samples was set to obtain nominal pore sizes of 350 and 500 μm for each of the patterns. Ten samples of each set were robocast and denoted as honeycomb_500; honeycomb_350; orthogonal_500; and, orthogonal_350. Finally, the 3D-printed structures were left to dry overnight at room temperature and afterwards pressure-less sintered (LH-300, LAC, Czech Republic) in air at 1200 °C for 5 h, using a heating rate of 2.5 $°C \cdot min^{-1}$.

2.3. Chemical and microstructural characterization

In order to identify the crystalline phases in the sintered samples, two cylinders were ground to be analyzed by powder X-ray diffraction (XRD) using a Rigaku SmartLab 3 kW apparatus. Scans were performed in Bragg–Brentano geometry between 10° and 90°, using Cu-Kα radiation ($\lambda = 0.154$ nm) at a current of 30 mA and 40 kV with a scan speed of $4° \cdot min^{-1}$. The Rietveld refinement was performed using the High Score Plus software (PANalytical B.V., The Netherlands, Version 3.0e) to determine the weight percentage of each crystalline compound.

The skeletal density of the sintered $CaSiO_3$–SiO_2 structures was determined by helium pycnometry (Micromeritics AccuPyc II 1340) and the specific surface area (SSA) was determined by nitrogen adsorption using the Brunauer-Emmett-Teller (BET) method (Autosorb iQ (Quantachrome Instruments, Boynton Beach, FL, USA). Prior to the measurement, the samples were degassed in vacuum at 180 °C for 12 h.

For the microstructural characterization, the upper surface of sintered samples was coated with a nanometric carbon layer to observe the microstructure by scanning electron microscopy (SEM; Lyra3, TESCAN). The final pore size of the sintered samples was measured by means of image analysis. Images were obtained at different magnifications and analyzed using the ImageJ software (FIJI, https://imagej.nih.gov/ij/index.html) in order to determine the average pore size for each arrangement, calculated by the distance between the filaments of a same deposited layer. Additionally, the porosity and pore size distribution of the sintered structures was measured and registered in the range between 0.09 and 1000 μm by mercury intrusion porosimetry (MIP, Quantachrome Poremaster, USA).

2.4. Differential thermal analysis and thermogravimetric essays

The thermal analysis of the calcined powder was carried out in order to identify energetic processes taking place during sintering. Simultaneous thermogravimetric analysis (TGA) and differential thermal analysis (DTA) were carried out in a Netzsch STA 409c/CD apparatus in a synthetic air atmosphere (14 vol % of O_2 in Ar) using Al_2O_3 crucibles with a heating rate of 10 $°C \cdot min^{-1}$ in the range of 20–1400 °C.

2.5. Mechanical characterization

Uniaxial compression test was performed using a universal testing machine (Instron 8874, USA) at a constant crosshead speed of 0.5 $mm \cdot min^{-1}$. The load was applied along the longitudinal axis of cylinders. The stress was calculated by dividing the applied force by the cross-section area of the sample. The compressive strength was equated to the maximum stress supported by the samples. Five samples were tested for each series and the mean values are reported with their standard deviations. The statistically significant differences between groups were determined by the *t*-test.

2.6. Assessment of active acid sites by NH_3 adsorption

The temperature-programmed desorption of ammonia (NH_3-TPD) experiments were carried out in a catalyst characterization instrument (AMI-90, Altamira Instruments, USA), equipped with a thermal conductivity detector (TCD) and coupled to a mass spectrometer (ThermoStar, Pfeiffer, USA). First, 50 mg of wollastonite–silica powder obtained from the grinding of porous structures (sintered at 1200 °C for 5 h) were thermally treated in Ar flow at 600 °C for 2 h in order to desorb the chemisorbed species in the material that might influence the NH_3 quantification. Later, the samples were exposed to an NH_3/He (5 vol % NH_3, 50 $cm^3 \cdot min^{-1}$) stream at 100 °C for 1 h. After purging the system with Ar to remove the physisorbed gas (weakly adsorbed at 100 °C for 1 h), the NH_3-TPD measurements were conducted incrementing the temperature up to 600 °C with a heating ramp of 10 $°C \cdot min^{-1}$. The quantities of chemisorbed NH_3 were obtained by integrating the areas under the peaks of the NH_3-TPD profiles and referenced to TCD signal calibrated for a known volume of NH_3. The classification of the acid-site strength was based on the desorption profile along the temperature range as follows: weak between 100 and 250 °C; medium from 250 to 400 °C; and strong above 400 °C.

2.7. Evaluation of catalytic activity by decomposition of isopropyl-alcohol vapor

The catalytic performance of the ground porous structures was tested using the isopropyl alcohol (IPA) decomposition as a model reaction. The catalytic conversion measurements were conducted in a fixed-bed reactor connected online to a gas chromatography system (HP 5890 Series II, HP, USA) equipped with a flame ionization detector (FID). In a typical experiment, 0.075 g of wollastonite-silica powder was deposited in a U-quartz reactor with an internal diameter of 8 mm, which was placed vertically inside a tubular furnace. Before the catalytic tests, the samples were pre-treated at 400 °C for 2 h with a pure N_2 stream (10 $cm^3 \cdot min^{-1}$) to desorb the chemisorbed species in the material that might have an impact on the results. Later, the system was cooled down to the reaction temperature under N_2 flow. The IPA (analytical reagent grade, purity ≥ 99.8%, Sigma Aldrich) was fed in gas phase (7.6×10^{-8} $mol \cdot s^{-1}$) using the N_2 stream through a saturator, which was maintained at 0 °C. Finally, the decomposition reaction was carried out in the temperature interval from 250 to 350 °C under atmospheric pressure. The progress of the IPA conversion into the corresponding decomposition products on the $CaSiO_3$–SiO_2 system was monitored by the gas chromatography system. The catalytic conversion (X) was calculated following equation (1) and the selectivity of the reaction (S_i) was estimated following equation (2):

$$X = \frac{M_o - M_f}{M_o}, \qquad \text{Eq.(1)}$$

$$S_i = \frac{M_i}{M_o - M_f}, \qquad \text{Eq.(2)}$$

where M_o is the molar flow of IPA initially introduced, M_f is the molar flow of IPA at the exit, and M_i is the molar flow of each product determined by the flame ionization detector (acetone or propylene).

3. Results

3.1. Crystalline phase composition

The XRD results of the as-obtained, calcined and sintered $CaSiO_3$–SiO_2 powders are shown in Fig. 1a. The as-obtained powder showed the characteristic pattern of an amorphous material

with some crystalline peaks attributed to the wollastonite. After calcination at 800 °C for 5 h, the partial crystallization of the amorphous powder was revealed by the sharping of the peaks, which mainly corresponded to wollastonite but also silica in its quartz polymorph. Furthermore, the hump in the XRD pattern indicates that an amorphous phase remained in the calcined powder. Finally, after sintering at 1200 °C for 5 h, the present crystalline phases were pseudowollastonite (Ps-wollastonite; PDF 01-089-6485) and two silica polymorphs, i.e., Cristobalite (PDF 01-076-0941) and Quartz (PDF 01-089-1961). Rietveld refinement of XRD patterns revealed that the sintered samples are composed of 53.9 wt % of Ps-wollastonite, 40.3 wt % of Cristobalite, and 5.8 wt % of high-temperature Quartz, resulting in a calcium silicate system with a skeletal density of 2.88 g·cm^{-3}.

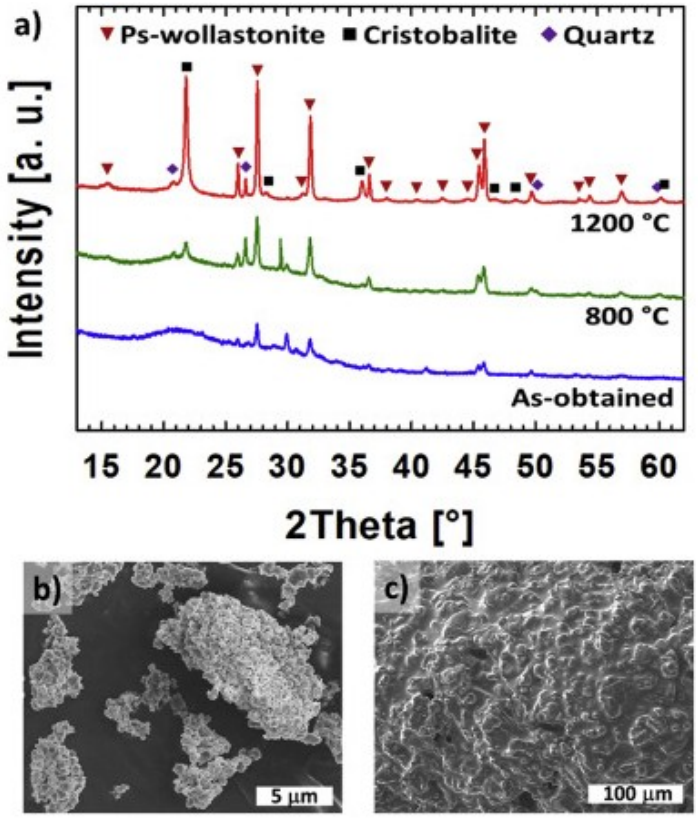

Fig. 1. a) X-ray diffraction patterns of the as-obtained powder, powder calcined at 800 °C for 5 h, and after sintering at 1200 °C for 5 h; b) initial morphology of as-obtained powder; c) characteristic surface microstructure of the robocast filaments that form the porous structures after sintering.

The morphology of the as-obtained powder is shown in Fig. 1b, revealing sub-micrometric particles forming agglomerates of several micrometers size. Fig. 1c shows the final surface microstructure after robocasting and sintering of the synthesized powder. The sintering mechanism appears to be promoted by a liquid or glass transition sintering, this is based on the visibly smooth surface of the filaments that surrounds bigger particles. However, the full densification of the filaments was not reached, since open pores with size below 10 µm can be found along the filaments. Such pores can be caused by the presence of trapped air during the paste preparation and/or extrusion during the robocasting process. The SSA of the sintered samples was in the range of 1–2 $m^2 \cdot g^{-1}$. Despite the values are close to the low detection limit of the technique, the honeycomb samples showed twice larger SSA (1.8 $m^2 \cdot g^{-1}$) than their orthogonal counterparts (0.8 $m^2 \cdot g^{-1}$).

3.2. Thermal phenomena occurring during sintering

TG/DTA curves of the synthesized powder after calcination at 800 °C for 5 h are shown in Fig. 2. The first endothermic phenomenon around 115 °C corresponds to desorption of water molecules accompanied by a mass loss of less than 0.5 wt %. Following that, a wide endothermic process was present up to around 500 °C that can be attributed to the slow quartz phase crystallization from the still present amorphous phase. In congruence with the pre-calcination of the powder, the total weight loss was around 2 wt %. Above 840 °C, an endothermic process took place, which is most probably initiated by the phase transformation of the quartz into tridymite and/or cristobalite phase. Above this temperature, the sample did not reveal any considerable weight change, thus, the mass was almost constant until the end of the measurement. Above 1100 °C, another endothermal transformation occurred, which is attributed to the restructuration of the wollastonite into pseudowollastonite [21] and it is in accordance with the XRD after the heat treatment at 1200 °C. The last endothermic process was registered around 1324 °C, which was probably caused by the glass transition of one of the present silica phases [22].

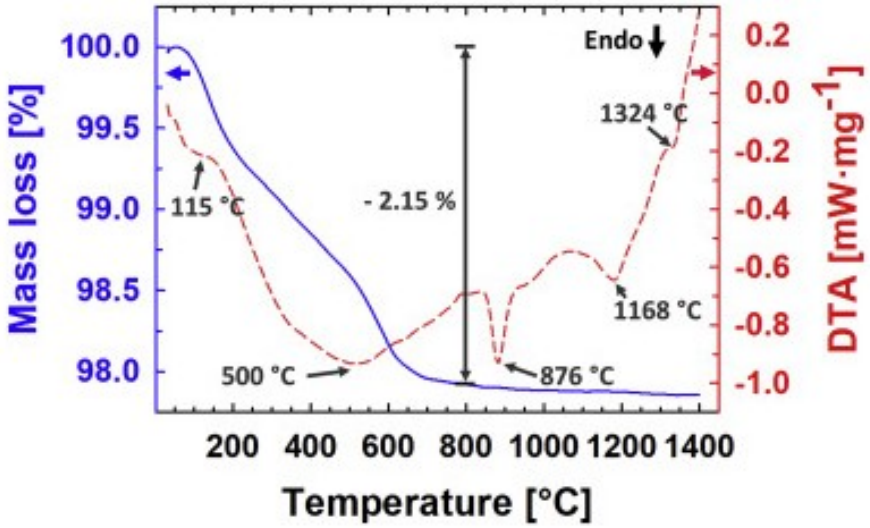

Fig. 2. Mass loss and DTA curve of pre-calcined wollastonite-silica powder.

3.3. Structural analysis of robocast $CaSiO_3$–SiO_2 samples

Characteristic SEM micrographs of the upper layer of $CaSiO_3$–SiO_2 samples are shown in Fig. 3 together with a close-up of the obtained pore geometry and the *in-silico* pattern projections in red. In addition, Table 1 summarizes the pore size, determined by image analysis and MIP, the final diameter of the filaments, the final diameter of the samples, and total porosity determined by MIP after the sintering for each of the arrangements.

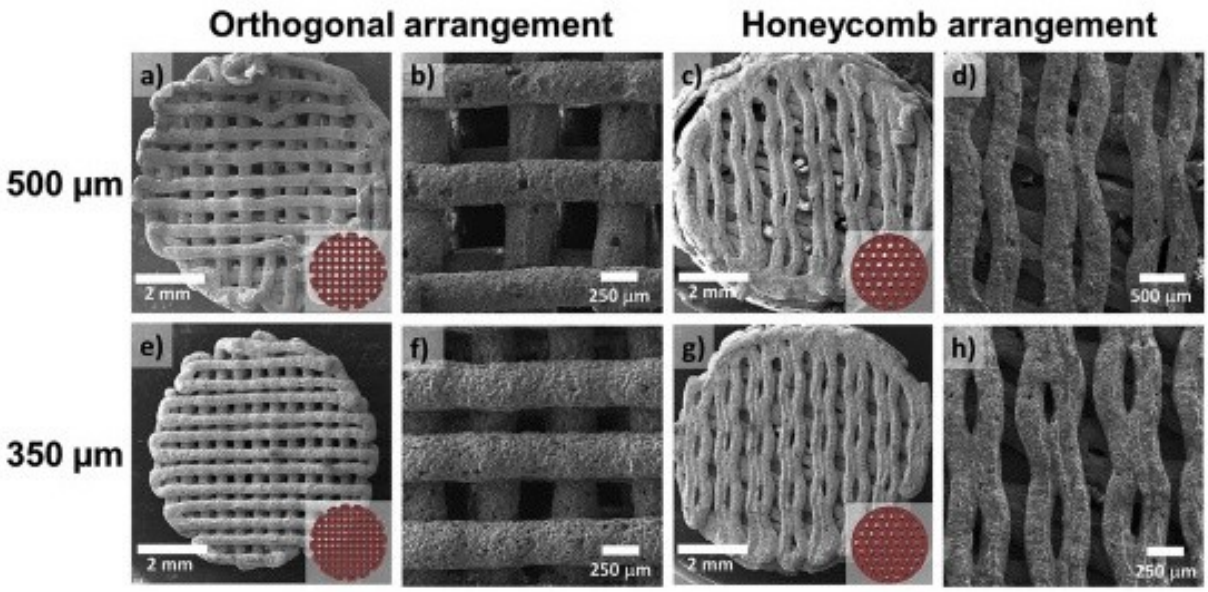

Fig. 3. Scanning electron micrographs of the robocast $CaSiO_3$–SiO_2 structures: a) and b) orthogonal 500-µm pore size; c) and d) honeycomb 500-µm pore size; e) and f) orthogonal 350-µm pore size; g) and h) honeycomb 350-µm pore size.

Table 1. Summary of the final dimensions and porosity of $CaSiO_3$–SiO_2 porous structures after sintering.

Arrangement	**Orthogonal**		**Honeycomb**	
Nominal pore size [µm]	500	350	500	350
Final pore size by image analysis [µm]	330 ± 60	230 ± 45	Minor axis: 167 ± 43 Major axis: 809 ± 159	Minor axis: 129 ± 22 Major axis: 646 ± 118
Mean macro-channel size by MIP [µm]	~326	~275	~245	~243
Final diameter of filaments [µm]	327 ± 12	312 ± 10	333 ± 11	332 ± 6
Final diameter of samples [mm]	8.0 ± 0.1	7.9 ± 0.1	7.9 ± 0.2	8.0 ± 0.1
Total porosity [%]	65.8	61.5	56.4	53.1

In comparison to the honeycomb pattern, the orthogonal arrangement was reproduced with a higher dimensional accuracy of the pore geometry. Despite that the filaments were deposited closer or farther to each other at some locations than prescribed in the *in-silico* pattern, the square shape of the pores was maintained along the whole samples (Fig. 3 a-b and 3 e-f). The average filament to filament aperture size was found to be 330 µm and 230 µm for the 500-µm and 350-µm nominal pore size structures, respectively (Table 1). These values were confirmed by MIP (Table 1 and Fig. 4). Furthermore, as the pore size was increased, i.e., nominally from 350 to 500 µm, the filaments bent due to the larger unsupported span. In contrast, the honeycomb pattern did not present any evident bending of the filaments, neither for 350 nor for 500 µm nominal pore size. This was because the layers in this arrangement were deposited one over the other with a 120-degree rotation between them, having a bigger amount of support material deposited in comparison to the orthogonal arrangement. The accuracy in the shape of the pores of the honeycomb arrangement was not in a good agreement with the *in-silico* models. Elliptical-like pores were obtained instead of hexagonal-like pores (Fig. 3 c-d and 3 g-h). Therefore, two pore sizes were measured, corresponding to

the minor and major axes of the elliptical pores (Table 1). In this case, the pore size (channel size) determined by MIP was considerably different than the two diameters of the ellipse determined by image analysis. However, as it can be observed in Fig. 4, the channels in the honeycomb pattern had a wider pore size distribution within the range of the values obtained by image analysis.

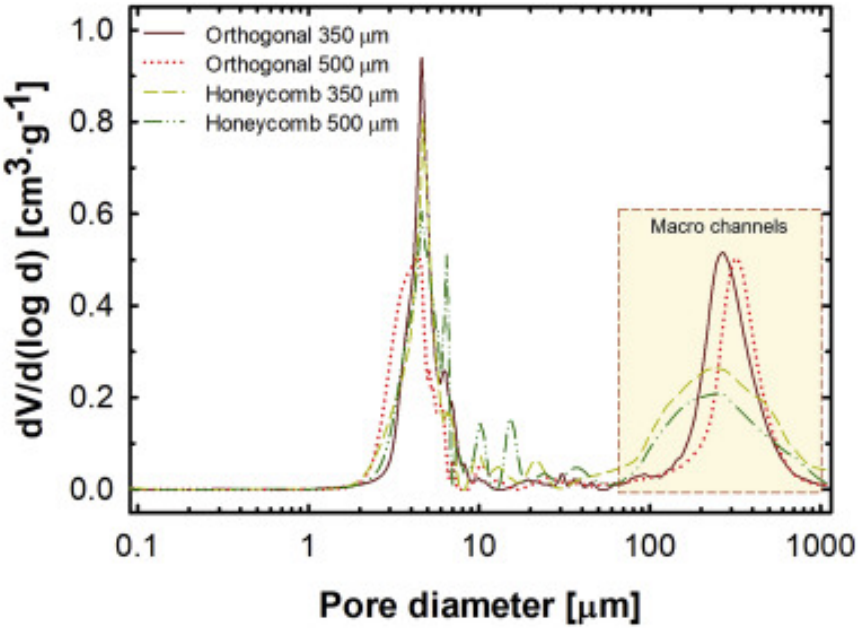

Fig. 4. Pore size distribution of the robocast $CaSiO_3$–SiO_2 structures with different pattern arrangements and different nominal distance between filaments.

In general, the shrinkage in the diameter of the samples was around 20 %, while the final diameter of the filaments was around 325 µm, similar values were observed for all the different structures.

The pore size distribution showed a bimodal distribution of pores in the samples (Fig. 4). While the pores centered on ~270 µm correspond to the spaces between deposited filaments, the pores centered on ~4–5 µm correspond to the open pores within the filaments. In general, the pore size distribution in the filaments was similar for all the patterns. In contrast, a clear difference was observed between honeycomb and orthogonal patterns in terms of the pore size distribution between filaments (macro channels). For the orthogonal arrangement, the distance between filaments showed a narrow distribution and the mean values for the two nominal sizes were different. In the case of the honeycomb arrangement, the pore size distribution was wider, with no clear shift of pore size. Moreover, the pore size distribution for the honeycomb samples showed the presence of some pores with size between 10 and 30 µm, which could be attributed to the lateral connections between the main channels of the structure.

3.4. Compression test

Porous structures with different arrangement and pore size were compared in terms of their compressive strength along the longitudinal axis (z-axis, Fig. 5a). The structures with honeycomb arrangement had more than threefold higher compressive strength than the orthogonal architecture (Fig. 5b). Furthermore, the variation in compressive strength was also larger for the honeycomb structures. This result is due to the more compact structure of the honeycomb pattern (Table 1) and different structure of load-bearing pillars, Fig. 5a.

Interestingly, the compressive strength of each design did not show statistically significant differences between the two studied pore sizes (Fig. 5b). Although the expected decrease in the average compressive strength with increasing pore size is apparent, more tests are needed to establish functional relationships.

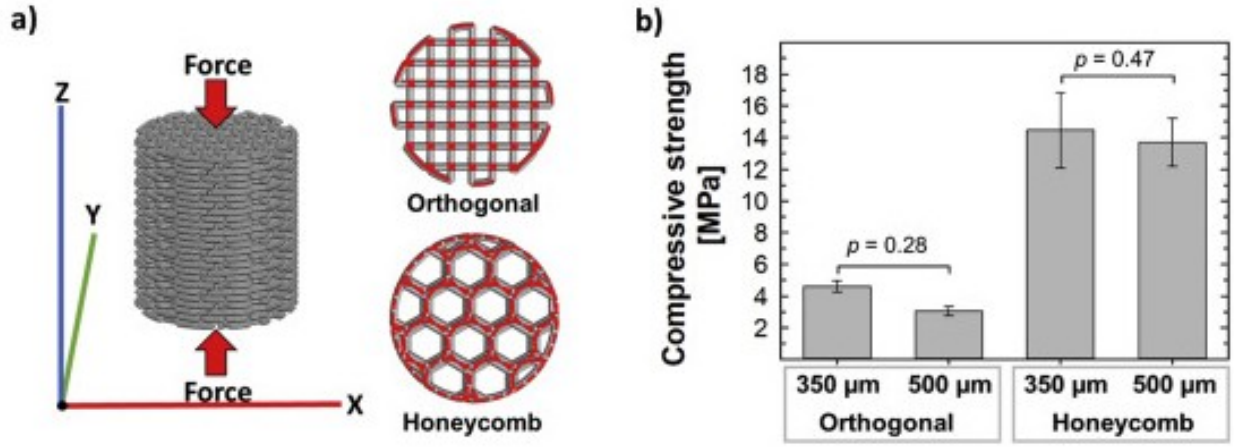

Fig. 5. a) Scheme showing the loading direction during the compression test. The effective area of the cross-section supporting the load is highlighted in red; b) mean compressive strength for different $CaSiO_3$–SiO_2 porous structures. (For interpretation of the references to colour in this figure legend, the reader is referred to the Web version of this article.)

3.5. Measurement of active sites by NH_3 temperature-programmed desorption (TPD)

The acidic property of the $CaSiO_3$–SiO_2 compound was evaluated by means of the quantification of the active sites with acidic nature. Table 2 shows the quantification of the active sites by the measurement of the desorbed NH_3 per gram of the material. The strength of the acid sites was qualitatively determined by the range of temperature to desorb the NH_3 molecules. Additionally, the NH_3-TPD profile is graphed in Fig. 6. Results showed that weak acid sites predominate in the $CaSiO_3$–SiO_2 system (4×10^{-3} mol per gram of the solid), followed by the strong active sites. The total number of active sites registered over the whole temperature interval (25–600 °C) was 9×10^{-3} mol·g^{-1}.

Table 2. Acid-site density for the $CaSiO_3$–SiO_2 system measured by NH_3 desorption concentration in a temperature range from 25 °C to 600 °C.

Temperature interval	NH_3 desorbed [mol·g^{-1}]	Adsorption force
25–250 °C	4×10^{-3}	Weak
250–400 °C	2×10^{-3}	Medium
400–600 °C	3×10^{-3}	Strong

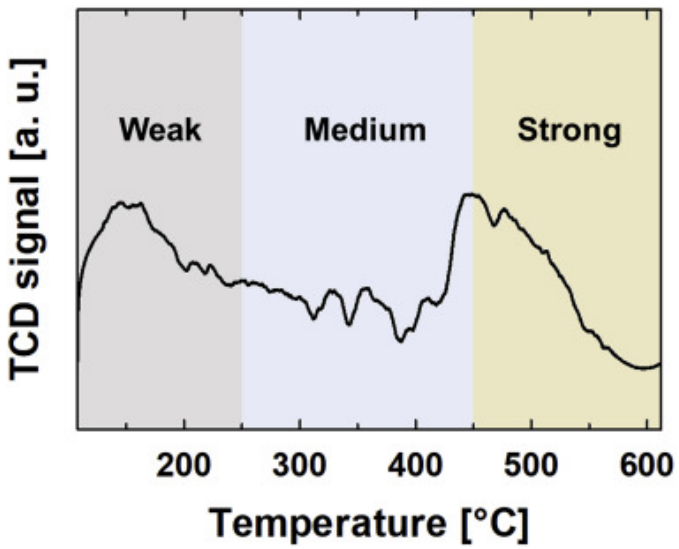

Fig. 6. Registered NH_3-TPD profile of 50 mg of $CaSiO_3$–SiO_2 (ground sintered structure). NH_3 adsorption force is classified by temperature range from weak to strong.

3.6. Catalytic decomposition of isopropyl-alcohol vapor

The effective catalytic properties of acid and base sites were assessed through the vapor-phase decomposition of IPA by ground powder obtained from the sintered robocast $CaSiO_3$–SiO_2 structures. Results showed that the IPA conversion increased with the temperature from around 0.46 at 250 °C to 0.92 at 350 °C (Fig. 7a), in accordance to an Arrhenius behavior, indicating that the mass-transfer limitations during the reactions were negligible. Only acetone and propylene were formed during the catalytic reaction.

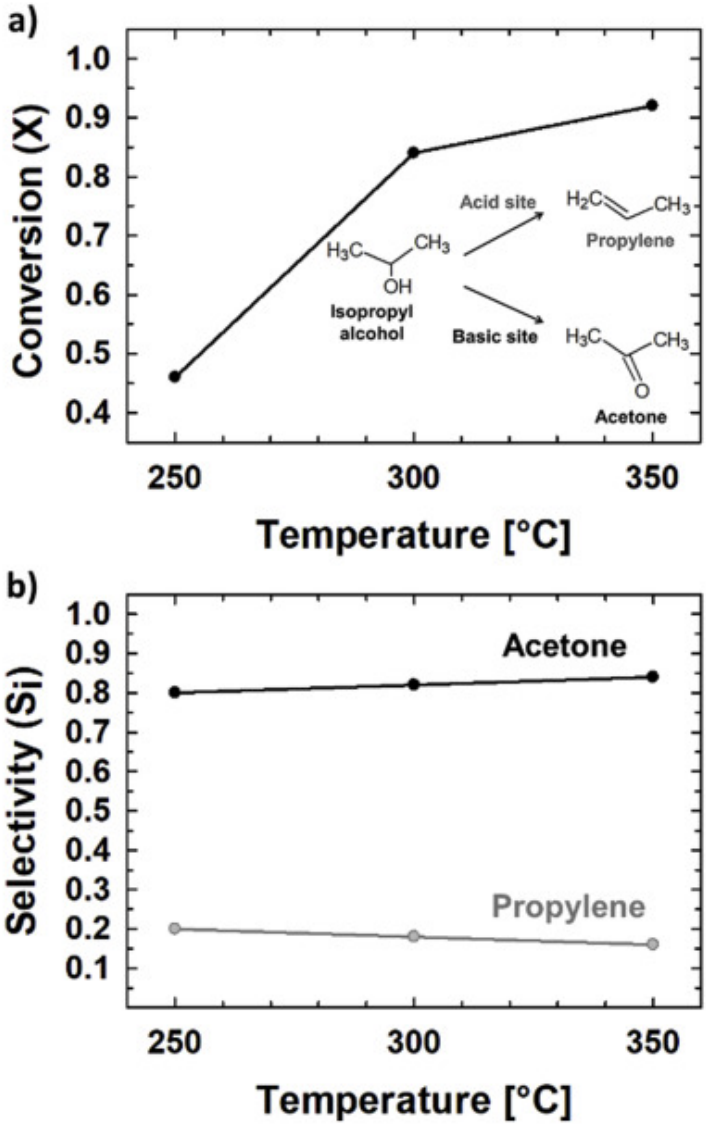

Fig. 7. a) Catalytic decomposition of isopropyl alcohol (IPA) by $CaSiO_3$–SiO_2 system at temperature range from 250 to 350 °C and schema of the decomposition of isopropyl alcohol depending on the acid or base properties of solid catalysts; and b) chemical reaction selectivity at different temperatures of the isopropyl alcohol decomposition into propylene and acetone.

The chemical reaction selectivity along the different temperatures is presented in Fig. 7b. The values indicate that the selectivity to produce acetone is higher than 80%. This result suggests a higher number of base-nature active centers than the previously measured acid sites, which are linked to the formation of propylene. The selectivity of both catalytic reactions was found nearly constant along the studied temperature range.

4. Discussion

The synthesis of wollastonite through wet chemistry involves a complex mechanism [23,24]. The synthesis of chemical-pure wollastonite must keep a Ca/Si ratio of 1:1. A small difference in the Ca/Si ratio leads to the precipitation of secondary phases as it can be observed in the binary phase diagram CaO–SiO_2 (Fig. 8) [25]. In this study, the co-precipitation method produced micro-agglomerates with Ca/Si ratio <1, which upon calcination produced

wollastonite with the presence of silica as α-cristobalite and β-quartz, which are stable at room temperature [26]. The crystallization of these two silica phases indicates the non-complete reaction between the Ca and Si ions to form wollastonite (Eq. (3)), accompanied by a simultaneous formation of silicon dioxide during the process. The remaining non-bonded Ca ions were most probably removed by the rinsing treatment before the calcination of the powder at 800 °C. Nevertheless, the presence of silica as a secondary product does not compromise the final use of the material, as silica and wollastonite are materials that share applications, e.g., catalysis, medicine, fillers for mechanical properties, water purification, among others [27, 28, 29].

Eq.(3)

$$Ca(NO_3)_2 + Si(OCH_3)_4 \xrightarrow{2\,NH_4OH} CaSiO_3 + 2\,NH_4NO_3 + 2\,C_2H_5OH + 2\,H_2O$$

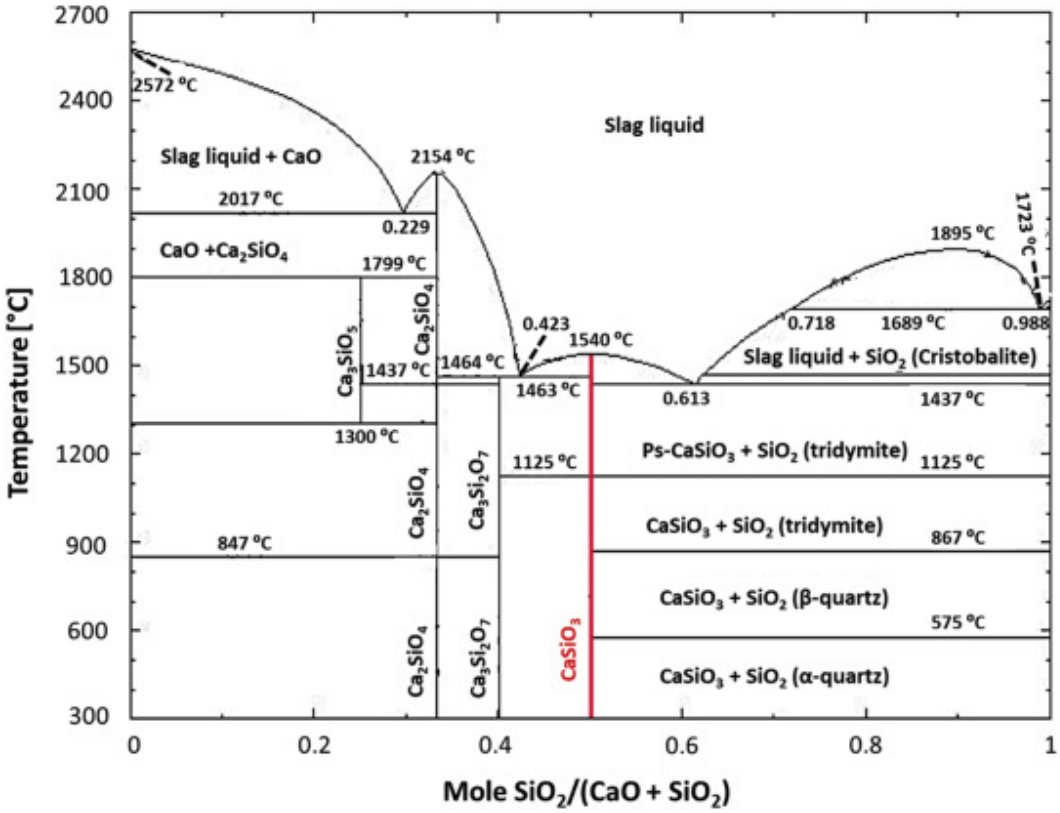

Fig. 8. CaO–SiO_2 phase diagram. Adapted from Ref. [25].

Even though the heat treatment during the sintering was carried out at 1200 °C, the cristobalite phase (high-temperature SiO_2 polymorph, above 1470 °C) was formed instead of the expected tridymite (low-temperature SiO_2 polymorph, 870 °C–1470 °C). Numerous investigations had reported that the presence of impurities can lead to the formation of cristobalite at lower temperatures [30, 31, 32, 33]. In the SiO_2 phase diagram, the first crystalline phase that forms when heating up amorphous silica is the α- and β-quartz (235 °C–870 °C), followed by the tridymite. However, the direct transition quartz → cristobalite [31] is reported in many studies without the transition quartz → tridymite → cristobalite, based on the intrinsic nature of the initial silica source, e.g., purity, particle size, crystal lattice

parameters and heat treatment [34, 35, 36, 37]. In addition, it is reported that the formation of cristobalite is considerably improved at temperatures higher than 1200 °C, temperature used for the sintering of the samples in the present work. Wollastonite, for its part, transforms to pseudowollastonite at ~1125 °C [21,38]; and at high temperatures (above 1200 °C) increases its activity as a flux material, decreasing the melting point or phase transition temperatures of the accompanying mineral material [39]. Thus, the presence of high-temperature phases is possible also in the $CaSiO_3$–SiO_2 composite system at low temperature.

The geometrical accuracy of the porous structures depends on the precision of the robocasting machine. In particular, the device used in the present work caused the filaments to be closer or farther to each other, varying the size of the cavities. Despite those shifts, the pore shape remained periodically homogenous along the whole samples. Moreover, it was observed that for the orthogonal arrangement, the geometry was better controlled than for the honeycomb architecture. In general, the honeycomb arrangement was found to have nearly two times higher shrinkage of pores compared to the orthogonal architecture, which can be caused by the initial shape of the pores. In the honeycomb structure, each layer is made of non-straight filaments in a distribution that creates ellipse-like pores. The staking of the elliptical pores in Z-direction creates channels along the axis of the cylindrical samples, with a few lateral connections between channels (Fig. 9) [40]. The elliptical shape of the pores results in a wider pore size distribution and the small lateral connections between channels are in the range of few tens of micrometers. In contrast, the pores in the orthogonal structure are formed by linear filaments rotated by 90° with respect to the previous layer, resulting in square-like pores. Similar to the honeycomb structure, the staking of pores in Z-direction creates channels that run along the axis of the cylindrical samples but they contain more lateral connections between channels (Fig. 9). The narrow pore size distribution of the orthogonal samples shows that the size of the channels is similar to the size of the lateral connections between channels.

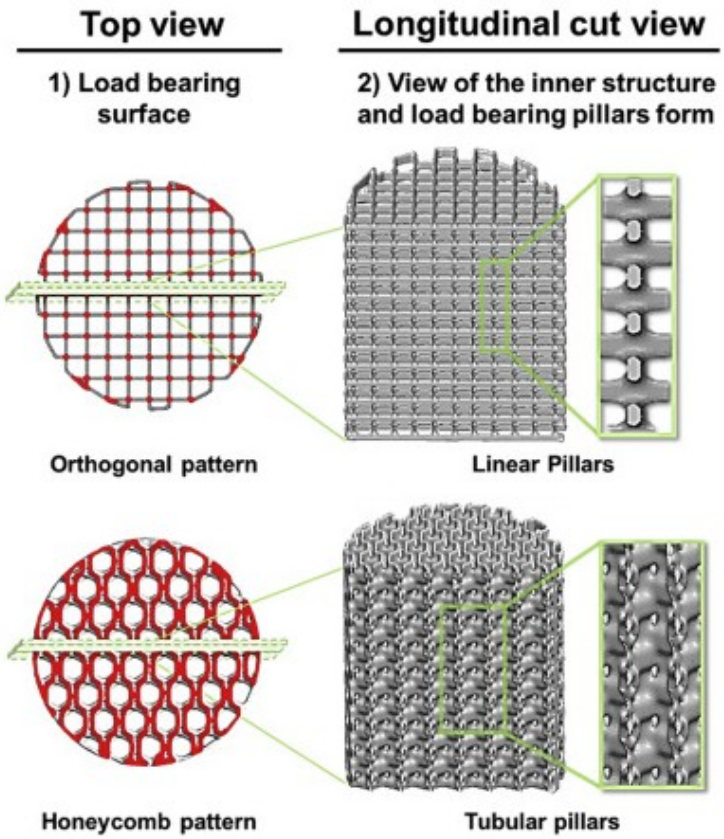

Fig. 9. The CAD model of porous structures with an orthogonal and honeycomb pattern. From left to right: 1) top view of the cylindrical structures with different patterns, load-bearing pillars under longitudinal compression are highlighted in red; 2) longitudinal cut through the patterns with a close-up of the formed channels and load-bearing pillars in the orthogonal and honeycomb pattern. (For interpretation of the references to colour in this figure legend, the reader is referred to the Web version of this article.)

Regarding the microstructure of the filaments, the sintering of the material was considered as semi-liquid sintering because the previous studies have reported that wollastonite decreases the glass transition temperature (Tg) of glass-ceramics [41,42], which might have happened for the silica. Therefore, a sintering mechanism controlled by mass transfer in liquid phase can be expected, which was confirmed by the smooth surface of the final filaments. Despite the fact that the semi-liquid sintering mechanism is considered beneficial for densification [43], the filaments of the sintered bodies still showed some remaining open pores. The porosity is something that can be controlled by varying the sintering conditions, depending if the pores within the filaments are desired or not for the final application.

As confirmed by the compression test, the consolidation of the 3D-plotted bodies resulted in relatively strong porous structures in all the cases. The mechanical strength depends mostly on the architecture pattern. The honeycomb arrangement was more than three times stronger than the orthogonal arrangement. This result is consistent with recent findings by Raymond et al. [40] and can be explained by the different geometry of load-bearing pillars formed by the staking of filaments in Z-direction. In the orthogonal arrangement, the pillars are based on consecutive crossings of perpendicular filaments. The pore channels in the Z-direction are regularly intersected by transverse pore channels, producing the 3D grid [40,44]. In contrast, the load-bearing pillars of the honeycomb structure are the walls of each elliptical unit, which have much lower transverse porosity (Fig. 8) [40,45]. This design is much more compact and leads to the higher stiffness and therefore the higher strength. However, geometrical irregularities resulting from the production process are also much more important in this case. When the compression load is applied longitudinally (perpendicular to the printing plane), the mechanical stability of the wall is affected by its imperfections. In the case of the orthogonal pattern, the longitudinal compression causes tension in individual filaments, which is highest at some distance from the joints [46]. The imperfections in the geometry of each filament and their alignment are less variable than the imperfection of much larger wall-like pillars and hence the variability of the compression strength is also lower. Consequently, when a more reliable design is required, the orthogonal pattern is more convenient. On the other hand, when higher strength is needed, the honeycomb architecture is more suitable. Furthermore, the two arrangements have pore channels suitable for gas transport in catalysis and showed similar SSA. However, a disadvantage of the studied structures is the low values of SSA which are considerably below the optimal for a catalyst but this can be improved by changing the sintering conditions or increasing the number of filaments in each layer.

After the optimization, the 3D-plotted $CaSiO_3$–SiO_2 structures can find their application as self-supporting catalytic structures, which may overcome the drawbacks of reactors that use packed beds of catalyst or inert structural supports coated with a thin layer of active material [47]. Either honeycomb or orthogonal structures fabricated on demand will avoid the use of inert support material, therefore no volume in the reactor will be lost. Regular structures will prevent pressure drops in the reactor while offering good mechanical, mass and heat transfer properties. Therefore, helping to make more efficient the use of the catalytic material.

The decomposition of IPA was studied as a preliminary proof of the effective catalytic properties of the $CaSiO_3$–SiO_2 system. The experiments were performed in grounded samples

instead of 3D structures with the aim to compare the results with previous results. The catalytic conversion of IPA occurs by two main pathways according to the chemical nature of the active sites in the catalyst. In the presence of acid sites, the dehydration of IPA produces propylene while in basic sites the dehydrogenation of IPA produces acetone [48]. This study showed that the basicity of the $CaSiO_3$–SiO_2 system was predominant, giving to the system high selectivity for basic-catalyzed processes. Therefore, the $CaSiO_3$–SiO_2 system can be used in catalytic processes such as amination, double bond migration, and alcohol condensation [49,50]. In fact, numerous studies have reported on the activity of calcium silicates as strong base catalysts or excellent substrates for several reactions related to the decomposition of oils for fuel production [51, 52, 53]. In addition, active metals can be incorporated as dopants or particles during the manufacturing to obtain complex catalysts, which can perform reactions where a bifunctional base-site/metal is required, for example in the hydrogenation of carbon monoxide for environmental applications [54].

Despite the strong base catalytic behavior in the $CaSiO_3$–SiO_2 system, the number of acid active sites with strong absorption force (4000 $\mu mol \cdot g^{-1}$) is higher compared to other single and combined oxide substrates reported in the literature, e.g., Al_2O_3, MgO, SiO_2, zeolites, etc. [47,50]. Those acid active sites can function as proton donors (Brønsted acid) or as electron-pair acceptors (Lewis acid), in both cases are useful as absorbents of heavy metals and ions or in selective cracking reactions [55].

5. Conclusions

Different design of patterns led to different degrees of accuracy of the pore geometry and size in the final robocast structures. An orthogonal pattern is more reproducible with better accuracy in comparison to the honeycomb arrangement. The mechanical strength can be tailored by the pattern used for the construction of the porous bodies. As it was registered, a honeycomb pattern exhibited almost three times higher compressive strength compared to the orthogonal pattern. The difference in the compressive strength is based on the porosity and geometry of pores, resulting in significantly different cross-sections. In the honeycomb pattern, dense tubular pillars are formed while in the orthogonal pattern thinner pillars are obtained.

The combination of $CaSiO_3$ together with SiO_2 leads to a synergetic combination for multiple applications. In the case of the catalytic study for the $CaSiO_3$–SiO_2 system exhibited high selective conversion of IPA into acetone with a yield up to 92% of total decomposition at 350 °C. This result demonstrates that this system can be used as a strong selective base-nature catalyst or function as a substrate for composed catalysts. Therefore, further analyses in porous calcium-silicate-based bodies are of high interest for many branches of the industry and research.

Declaration of competing interest

The authors declare that they have no known competing financial interests or personal relationships that could have appeared to influence the work reported in this paper.

Acknowledgements

This project has received funding from the Brno University of Technology - BUT Internal Projects: STI-J-18-5456, Czechia. Authors also acknowledge the project CEITEC 2020 (LQ1601) with financial support from the Ministry of Education, Youth and Sports of the Czech Republic under the National Sustainability Program II, Czechia. Part of the work was carried out with the support of core facilities of research infrastructure CEITEC Nano RI, MEYS CR, 2016–2019, Czechia. EBM acknowledges the CONACYT grant 2018-000022-01EXTV-00188, Mexico.

References

[1] R.P. Sreekanth Chakradhar, B.M. Nagabhushana, G.T. Chandrappa, K.P. Ramesh, J.L. Rao, Solution combustion derived nanocrystalline macroporous wollastonite ceramics, Mater. Chem. Phys., 95 (2006), pp. 169-175, 10.1016/J.MATCHEMPHYS.2005.06.002

[2] M. VUKOVICH Jr., Effect of wollastonite substitutions in a semivitreous dinnerware body, J. Am. Ceram. Soc., 39 (1956), pp. 323-329, 10.1111/j.1151-2916.1956.tb15597.x

[3] A.J. Allen, J.J. Thomas, H.M. Jennings, Composition and density of nanoscale calcium–silicate–hydrate in cement, Nat. Mater., 6 (2007), p. 311, 10.1038/nmat1871

[4] G. Chen, L. Shi, Removal of Cd(ii) and Pb(ii) ions from natural water using a low-cost synthetic mineral: behavior and mechanisms, RSC Adv., 7 (2017), pp. 43445-43454, 10.1039/C7RA08018B

[5] N. Obradović, S. Filipović, S. Marković, M. Mitrić, J. Rusmirović, A. Marinković, V. Antić, V. Pavlović, Influence of different pore-forming agents on wollastonite microstructures and adsorption capacities, Ceram. Int., 43 (2017), pp. 7461-7468, 10.1016/J.CERAMINT.2017.03.021

[6] Y.C. Sharma, G.S. Gupta, G. Prasad, D.C. Rupainwar, Use of wollastonite in the removal of Ni(II) from aqueous solutions, Water. Air. Soil Pollut., 49 (1990), pp. 69-79, 10.1007/BF00279511

[7] M. Abdel Wahab, I. Abdel Latif, M. Kohail, A. Almasry, The use of Wollastonite to enhance the mechanical properties of mortar mixes, Constr. Build. Mater., 152 (2017), pp. 304-309, 10.1016/J.CONBUILDMAT.2017.07.005

[8] F. Zhang, J. Chang, K. Lin, J. Lu, Preparation, mechanical properties and in vitro degradability of wollastonite/tricalcium phosphate macroporous scaffolds from nanocomposite powders, J. Mater. Sci. Mater. Med., 19 (2008), pp. 167-173, 10.1007/s10856-006-0056-3

[9] X. Liu, M. Morra, A. Carpi, B. Li, Bioactive calcium silicate ceramics and coatings, Biomed. Pharmacother., 62 (2008), pp. 526-529, 10.1016/J.BIOPHA.2008.07.051

[10] H. Shao, Y. He, J. Fu, D. He, X. Yang, J. Xie, C. Yao, J. Ye, S. Xu, Z. Gou, 3D printing magnesium-doped wollastonite/β-TCP bioceramics scaffolds with high strength and adjustable degradation, J. Eur. Ceram. Soc., 36 (2016), pp. 1495-1503, 10.1016/J.JEURCERAMSOC.2016.01.010

[11] T.V. Vakalova, V.M. Pogrebenkov, N.P. Karionova, Solid-phase synthesis of wollastonite in natural and technogenic siliceous stock mixtures with varying levels of calcium carbonate component, Ceram. Int., 42 (2016), pp. 16453-16462, 10.1016/J.CERAMINT.2016.06.060

[12] R. Abd Rashid, R. Shamsudin, M.A. Abdul Hamid, A. Jalar, Low temperature production of wollastonite from limestone and silica sand through solid-state reaction, J. Asian Ceram. Soc., 2 (2014), pp. 77-81, 10.1016/J.JASCER.2014.01.010

[13] H. Wang, Q. Zhang, H. Yang, H. Sun, Synthesis and microwave dielectric properties of CaSiO3 nanopowder by the sol–gel process, Ceram. Int., 34 (2008), pp. 1405-1408, 10.1016/J.CERAMINT.2007.05.001

[14] E.R. Essien, E.E. Kaufmann, Luqman A. Adams, A new route to sol-gel crystalline wollastonite bioceramic, J. Asian Ceram. Soc., 6 (2018), pp. 132-138, 10.1080/21870764.2018.1480685

[15] K. Lin, J. Chang, J. Lu, Synthesis of wollastonite nanowires via hydrothermal microemulsion methods, Mater. Lett., 60 (2006), pp. 3007-3010, 10.1016/J.MATLET.2006.02.034

[16] R. Morsy, R. Abuelkhair, T. Elnimr, A facile route to the synthesis of hydroxyapatite/wollastonite composite powders by a two-step coprecipitation method, Silicon, 9 (2017), pp. 637-641, 10.1007/s12633-015-9339-y
[17] J. Zhao, Z. Wang, L. Wang, H. Yang, M. Zhao, The synthesis and characterization of TiO2/wollastonite composite, Mater. Lett., 37 (1998), pp. 149-155, 10.1016/S0167-577X(98)00079-2
[18] L.C. Hwa, S. Rajoo, A.M. Noor, N. Ahmad, M.B. Uday, Recent advances in 3D printing of porous ceramics: a review, Curr. Opin. Solid State Mater. Sci., 21 (2017), pp. 323-347, 10.1016/J.COSSMS.2017.08.002
[19] S. Somiya, T. OhjiPorous ceramic materials, handb, Adv. Ceram. (2013), pp. 1131-1148, 10.1016/B978-0-12-385469-8.00059-9
[20] J.A. Lewis, Direct ink writing of 3D functional materials, Adv. Funct. Mater., 16 (2006), pp. 2193-2204, 10.1002/adfm.200600434
[21] H. Yang, C.T. Prewitt, On the crystal structure of pseudowollastonite (CaSiO3), Am. Mineral., 84 (1999), pp. 929-932, 10.2138/am-1999-5-629
[22] R. Brückner, Properties and structure of vitreous silica. I, J. Non-Cryst. Solids, 5 (1970), pp. 123-175, 10.1016/0022-3093(70)90190-0
[23] I.G. Richardson, The calcium silicate hydrates, Cement Concr. Res., 38 (2008), pp. 137-158, 10.1016/J.CEMCONRES.2007.11.005
[24] E. Tajuelo Rodriguez, K. Garbev, D. Merz, L. Black, I.G. Richardson, Thermal stability of C-S-H phases and applicability of Richardson and Groves' and Richardson C-(A)-S-H(I) models to synthetic C-S-H, Cement Concr. Res., 93 (2017), pp. 45-56, 10.1016/J.CEMCONRES.2016.12.005
[25] E.F. Nordstrand, A.N. Dibbs, A.J. Eraker, U.J. Gibson, Alkaline oxide interface modifiers for silicon fiber production, Opt. Mater. Express, 3 (2013), pp. 651-657, 10.1364/OME.3.000651
[26] H. AOKI, S. TSUNEYUKI, Silica polymorphs, Nature, 340 (1989), p. 193, 10.1038/340193b0
[27] N.S. Lani, N. Ngadi, N.Y. Yahya, R.A. Rahman, Synthesis, characterization and performance of silica impregnated calcium oxide as heterogeneous catalyst in biodiesel production, J. Clean. Prod., 146 (2017), pp. 116-124, 10.1016/J.JCLEPRO.2016.06.058
[28] S.H. Abd El Rahim, A.A. Melegy, E.M.A. Hamzawy, Wollastonite-pseudowollastonite from silica fume, limestone and glass cullet composite, Interceram - Int. Ceram. Rev., 66 (2017), pp. 232-236, 10.1007/BF03401217
[29] A. Santos, J.A. Toledo-Fernández, R. Mendoza-Serna, L. Gago-Duport, N. de la Rosa-Fox, M. Piñero, L. Esquivias, Chemically active silica Aerogel−Wollastonite composites for CO2 fixation by carbonation reactions, Ind. Eng. Chem. Res., 46 (2007), pp. 103-107, 10.1021/ie0609214
[30] O. Şan, C. Özgür, Investigation of a high stable β-cristobalite ceramic powder from CaO–Al2O3–SiO2 system, J. Eur. Ceram. Soc., 29 (2009), pp. 2945-2949, 10.1016/J.JEURCERAMSOC.2009.04.013
[31] L. Pagliari, M. Dapiaggi, A. Pavese, F. Francescon, A kinetic study of the quartz–cristobalite phase transition, J. Eur. Ceram. Soc., 33 (2013), pp. 3403-3410, 10.1016/J.JEURCERAMSOC.2013.06.014
[32] A.J. Perrotta, D.K. Grubbs, E.S. Martin, N.R. Dando, H.A. McKinstry, C.-Y. HuargChemical stabilization of β-cristobalite, J. Am. Ceram. Soc., 72 (1989), pp. 441-447, 10.1111/j.1151-2916.1989.tb06150.x
[33] E.S. Thomas, J.G. Thompson, R.L. Withers, M. Sterns, Y. Xiao, R.J. Kirkpatrick, Further investigation of the stabilization of β-cristobalite, J. Am. Ceram. Soc., 77 (1994), pp. 49-56, 10.1111/j.1151-2916.1994.tb06956.x

[34] L. Dubrovinsky, N. Dubrovinskaia, S. Saxena, F. Tutti, S. Rekhi, T. Le Bihan, G. Shen, J. Hu, Pressure-induced transformations of cristobalite, Chem. Phys. Lett., 333 (2001), pp. 264-270, 10.1016/S0009-2614(00)01147-7
[35] N.A. Dubrovinskaia, L.S. Dubrovinsky, S.K. Saxena, F. Tutti, S. Rekhi, T. Le Bihan, Direct transition from cristobalite to post-stishovite alpha-PbO2-like silica phase, Eur. J. Mineral., 13 (2001), pp. 479-483, 10.1127/0935-1221/2001/0013-0479
[36] L. Sapei, R. Nöske, P. Strauch, O. Paris, Isolation of mesoporous biogenic silica from the perennial plant equisetum hyemale, Chem. Mater., 20 (2008), pp. 2020-2025, 10.1021/cm702991f
[37] D.R. Bassett, E.A. Boucher, A.C. Zettlemoyer, The effect of alkali halides and silver nitrate on the crystallization of silica powders, J. Mater. Sci., 7 (1972), pp. 1379-1382, 10.1007/BF00574929
[38] V. Swamy, L.S. Dubrovinsky, Thermodynamic data for the phases in the CaSiO3 system, Geochem. Cosmochim. Acta, 61 (1997), pp. 1181-1191, 10.1016/S0016-7037(96)00403-6
[39] S.R. Bragança, H.C.M. Lengler, C.P. Bergmann, Wollastonite as a flux for ceramics bodies, Mater. Sci. Forum, 727–728 (2012), pp. 1016-1021
https://doi.org/10.4028/www.scientific.net/MSF.727-728.1016
[40] S. Raymond, Y. Maazouz, E.B. Montufar, R.A. Perez, B. González, J. Konka, J. Kaiser, M.-P. Ginebra, Accelerated hardening of nanotextured 3D-plotted self-setting calcium phosphate inks, Acta Biomater., 75 (2018), pp. 451-462, 10.1016/J.ACTBIO.2018.05.042
[41] O. Turkmen, A. Kucuk, S. Akpinar, Effect of wollastonite addition on sintering of hard porcelain, Ceram. Int., 41 (2015), pp. 5505-5512, 10.1016/J.CERAMINT.2014.12.126
[42] M. Magallanes-Perdomo, P. Pena, P.N. De Aza, R.G. Carrodeguas, M.A. Rodríguez, X. Turrillas, S. De Aza, A.H. De Aza, Devitrification studies of wollastonite–tricalcium phosphate eutectic glass, Acta Biomater., 5 (2009), pp. 3057-3066, 10.1016/J.ACTBIO.2009.04.026
[43] R.M. German, P. Suri, S.J. Park, Review: liquid phase sintering, J. Mater. Sci., 44 (2009), pp. 1-39, 10.1007/s10853-008-3008-0
[44] P. Miranda, A. Pajares, F. Guiberteau, Finite element modeling as a tool for predicting the fracture behavior of robocast scaffolds, Acta Biomater., 4 (2008), pp. 1715-1724, 10.1016/J.ACTBIO.2008.05.020
[45] B. Panda, M. Leite, B.B. Biswal, X. Niu, A. Garg, Experimental and numerical modelling of mechanical properties of 3D printed honeycomb structures, Measurement, 116 (2018), pp. 495-506, 10.1016/J.MEASUREMENT.2017.11.037
[46] P. Skalka, K. Slámečka, E.B. Montufar, L. Čelko, Estimation of the effective elastic constants of bone scaffolds fabricated by direct ink writing, J. Eur. Ceram. Soc., 39 (2019), pp. 1586-1594, 10.1016/J.JEURCERAMSOC.2018.12.024
[47] J. Lefevere, S. Mullens, V. Meynen, The impact of formulation and 3D-printing on the catalytic properties of ZSM-5 zeolite, Chem. Eng. J., 349 (2018), pp. 260-268, 10.1016/J.CEJ.2018.05.058
[48] E. Jasińska, B. Krzyżyńska, M. Kozłowski, Activated carbon modified with different chemical agents as a catalyst in the dehydration and dehydrogenation of isopropanol, Catal. Lett., 125 (2008), pp. 145-153, 10.1007/s10562-008-9536-z
[49] H. HattoriHeterogeneous basic catalysis, Chem. Rev., 95 (1995), pp. 537-558, 10.1021/cr00035a005
[50] A. Gervasini, J. Fenyvesi, A. Auroux, Study of the acidic character of modified metal oxide surfaces using the test of isopropanol decomposition, Catal. Lett., 43 (1997), pp. 219-228, 10.1023/A:1018979731407

[51] S. Sanna, W.G. Schmidt, P. Thissen, Formation of hydroxyl groups at calcium-silicate-hydrate (C-S-H): coexistence of Ca–OH and Si–OH on wollastonite(001), J. Phys. Chem. C, 118 (2014), pp. 8007-8013, 10.1021/jp500170t
[52] R.M. Srivastava, K.K. Panday, V.N. Singh, S.K. Khare, Removal of basic dye (crystal violet) from water using wollastonite as adsorbent, Environ. Technol. Lett., 9 (1988), pp. 1163-1172, 10.1080/09593338809384678
[53] H.I. El Shimi, N.K. Attia, G.I. El Diwani, S.T. El Sheltawy, Investigation of silicates as a catalyst in biodiesel production: a review, Int. J. Energy Res., 40 (2016), pp. 1743-1756, 10.1002/er.3546
[54] A. Holmen, D. Schanke, G. Sundmark, Hydrogenation of carbon monoxide over iron catalysts on different supports, Appl. Catal., 50 (1989), pp. 211-221, 10.1016/S0166-9834(00)80837-4
[55] F. Trejo, M.S. Rana, A. Rueda, Hydrotreating catalysts on different supports and its acid–base properties, Fuel, 100 (2012), pp. 163-172, 10.1016/J.FUEL.2012.04.026